Article

Wind Turbine Blade Design Optimization for Reduced *LCoE*, Focusing on Design-Driving Loads Due to Storm Conditions

Giannis Serafeim [1,*], Dimitris Manolas [1,2], Vasilis Riziotis [1] and Panagiotis Chaviaropoulos [2]

1   School of Mechanical Engineering, National Technical University of Athens (NTUA), GR 15780 Athens, Greece
2   iWind Renewables Private Company, GR 15344 Athens, Greece
*   Correspondence: seraf@fluid.mech.ntua.gr

Abstract: Design modifications of the blade inner structure, targeted at reducing design-driving extreme loads due to storm conditions, are assessed in the present paper. Under survival wind speeds, the lack of sufficient aerodynamic damping in the edgewise direction is responsible for excessive stall-induced vibrations that usually drive wind turbine blade design loads. The modifications considered in the work are (i) a non-symmetric increase in the thickness of the uniaxial and tri-axial material on the suction and pressure side of the blade sections, (ii) a shift in the spar caps in opposite directions and (iii) the ply-angle re-orientation of the laminates on the spar caps. The first two design interventions aim at increasing the damping of the low-damped edgewise modes in the idling rotor, while the third aims at reducing the fatigue and ultimate loads in normal operation. The design parameters in the problem are determined on the basis of a multidisciplinary optimization (MDAO) process, which minimizes the levelized cost of energy (*LCoE*). The in-house integrated optimization tool employed in the present study combines: (i) a servo-aero-elastic analysis tool for calculating ultimate loads and power yield, (ii) a cross-sectional analysis tool for obtaining structural properties and stress distributions in the modified blades and (iii) a cost model of the overall wind turbine to evaluate the *LCoE*.

Keywords: aeroelastic optimization; levelized cost of energy (*LCoE*); passive load control; flap-edge coupling; multidisciplinary aeroelastic optimization

1. Introduction

In the design phase of a wind turbine blade, manufacturers often deal with the situation that their new blade design withstands extreme operational loads but fails to withstand loads due to survival wind, when in parked or idling mode. Parked or idling rotors, experiencing extreme wind speeds, are likely to encounter high angles of attack within the post-stall region [1]. Whether these high angles of attack will appear depends on the inclination of the topography, the tilt angle of the nacelle, as well as the yaw misalignment of the inflow, static or dynamic (due to the wind turbulence). Such high angles of attack may give rise to stall-induced, edgewise vibrations on the blades, which, on many occasions, drive the design loads. These load-driving design load cases (DLCs) are designated in the IEC 61400-1 [2] standard by the code name DLC-6.x. They include parked or/and idling cases at extreme wind speeds, which are either combined (DLC-6.2) or not (DLC-6.1), with some failure of the grid or malfunctioning of the control system. A typical fault for wind turbines is the loss of the grid connection, combined with a failure in the Uninterrupted Power Supply (UPS) system. In this circumstance, the rotor fails to track the wind and, therefore, high yaw misalignment angles and high angles of attack in deep stall may occur. A similar condition can be encountered during the installation of the turbine before its electrification.

Aeroelastic simulations of idling rotors indicate that maximum blade loads (combined bending moments) appear for yaw angles in the ranges $(-40°, -15°)$ or $(15°, 40°)$ [1].

Yaw misalignment angles of $-/+15°$ are likely to occur even in normal idling operation (DLC-6.1), while higher yaw angles can only be encountered as a result of some fault in the wind-tracking system (DLC-6.2). Aerodynamic loads in such conditions (i.e., in deep stall) can be accurately estimated using engineering tools that rely on tabulated airfoil data (i.e., the so-called polars), only if a valid dynamic stall model is employed. Nevertheless, the uncertainty in the prediction of the aerodynamic loads in dynamic stall is a well-known fact within the wind energy sector [3–5] and it is the main cause of the consequent uncertainty in the prediction of the stall-induced edgewise vibrations. Different state-of-the-art dynamic stall models (e.g., Beddoes–Leishman [6] and ONERA [7]) can give significantly different load results in the onset of dynamic stall due to the quite different aerodynamic damping predicted by the stall models. Therefore, extreme loads of an idling rotor might substantially deviate, especially when the overall aerodynamic damping of certain modes of the system is very low or even negative. This explains why a blade that has been designed using a specific dynamic stall model may appear not to be able to withstand the loads of DLCs-6.x when a different dynamic stall model is considered. However, it is not easy to identify which model is the most appropriate for idling rotor analyses or which model provides the most conservative predictions. Dynamic stall measurements at very high angles of attack that could be used as a means to calibrate engineering state-of-the-art dynamic stall models are scarce.

One possible remedy for mitigating the above-discussed uncertainty in load prediction is to tailor the blade design in such a way that the damping of the poorly damped edgewise modes is enhanced. The results of the different dynamic stall models tend to converge when the damping of the rotor modes is well above the onset of the instability. An effective way to enhance the damping of the poorly damped edgewise modes is by means of Flap Edge Coupling (FEC). Previous studies [8] have shown that, under certain conditions, the coupling of the edgewise and flapwise motion, in the low-damped edgewise modes, increases their aerodynamic damping. The most effective way to enhance FEC is to increase the blade's structural twist angle, which is achieved by enhancing the cross-bending stiffness along the blade span.

When manufacturers come across the abovementioned problem, i.e., that DLC-6.x loads exceed the strength limits of their design, they usually apply ad hoc, local modifications, e.g., locally reinforcing the inner-blade structure in order to increase strength margins. Such modifications, although solving the problem, increase the weight of the blade, which is by no means optimum. Even if they decide to increase the blade's structural twist in order to enhance the damping of the edgewise rotor modes, this is also usually done non-optimally, through local interventions in the inner structure of the blade, e.g., by increasing the thickness of the composite material towards the leading edge on the suction side and towards the trailing edge on the pressure side. However, an unbounded increase in FEC could entail implications in the operational loads. Blades with enhanced FEC, under the action of extreme flapwise loads, usually tend to undergo high leading edgewise deflections, which make the blade behave as a virtually forward swept blade. As a result of the forward sweep, the blade tends to twist towards stall and, therefore, to further increase the flapwise loading in normal operation.

A consistent and effective way to tailor the wind turbine blades is to determine the parameters in the design problem within the course of an optimization process. Within such an optimization loop, the best combination of design variables is sought that mitigates stall-induced vibrations without deteriorating normal operation loading, using, as objective functions, some design cost parameter. This is the approach adopted in the present work. Two different FEC methods are employed for the idling DTU-10MW Reference Wind Turbine (RWT) [9] in order to mitigate stall-induced edgewise vibrations. The first FEC method considered is the one typically employed by wind turbine manufacturers. The thicknesses of the blade section walls are varied asymmetrically between the suction and the pressure side. Higher thicknesses of the uniaxial (UNIAX) and triaxial (TRIAX) composite materials is considered towards the leading edge (LE) of the section on its suction side

(segment "leading" of L/P side in Figure 1, left), while the thickness of the walls on the pressure side is reinforced towards the trailing edge (TE) (segment "trailing" of H/P side in Figure 1, left). The second method is first addressed by the authors in [10] and it consists of shifting the two spar caps in opposite directions. The spar cap on the suction side is displaced towards the LE, while the spar cap on the pressure side is displaced towards the TE (as illustrated in Figure 1, right).
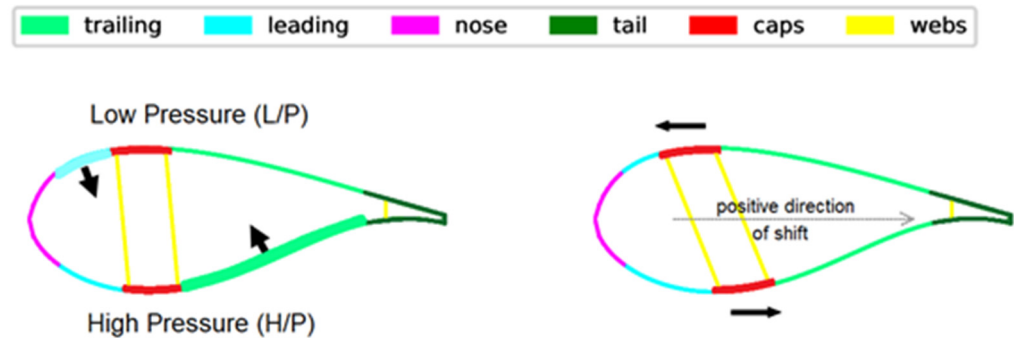

Figure 1. Definition of blade cross-section, demonstrating the material (**left**) and geometrically (**right**) based FEC through appropriate asymmetric thickness increase or displacement of the spar caps.

The design parameters in both methods are optimized within a MDAO loop, in which the objective function is the overall *LCoE* of the wind turbine. The assessment of the potential design solutions considers both the critical survival wind load cases but also the most critical operational load cases, with the aim to ensure that design modifications that improve the loading of the idling rotor do not entail a deterioration in the operational loading characteristics. The last step of the optimization analyses is to combine both FEC methods and, at the same time, apply a moderate material Bend Twist Coupling (BTC) [11,12] through the introduction of an offset angle to the composite plies of the uniaxial (UNIAX) material over the spar caps of the blade (as illustrated in Figure 2), aiming at compensating any increase in the operational loads due to FEC. The constraint in the optimization process is the requirement that the maximum obtained Tsai–Hill criterion values in the optimum design [13] do not exceed those of the reference blade considering only operational ultimate loads. This is a deliberate choice, which entails a more conservative design than the one that satisfies the requirement that Tsai–Hill values do not exceed the unit failure threshold. However, it is a choice that ensures that the optimum blade design is directly comparable to the reference blade.
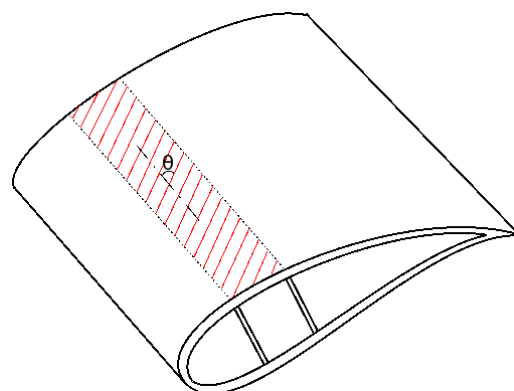

Figure 2. Definition of ply offset angle θ of fibre orientation (mirror lay-up) of uni-directional material on the spar caps of material BTC blades.

The MDAO framework used in the present study consists of the following in-house or freely available modules:

- The in-house hydro-servo-aero-elastic tool hGAST [14,15], which simulates the full wind turbine system at all operational conditions of interest and provides ultimate resultant internal loads (reaction forces and moments over the various components in the wind turbine) and power yield.
- A cross-sectional analysis tool [10] based on thin lamination theory [16], which provides stress distributions and values of the Tsai–Hill failure criterion over the various cross-sections in the structure. The cross-sectional tool takes, as input, the resultant ultimate internal loads generated by hGAST. The same module calculates beam cross-sectional properties in the different components, considering, as input, the material structural properties, thickness and distribution of stresses over every cross-section.
- A cost model that determines the cost of the full wind turbine system based on existing data available in the literature [17], as well as on empirical formulae, which specify certain cost parameters as a function of the component dimensions.
- An optimization framework based on ready-made functions from the publicly available scipy library in Python [18].

The contribution of the present paper lies in the design of wind turbine blades within an MDAO loop that are optimized for *LCoE* and account for the design-driving loads due to storm conditions. The aero-elastically tailored rotor blades combine both FEC and BTC passive control techniques, the first for enhancing stability in idling operation at survival wind speeds and the second for reducing loads in normal operation. Furthermore, two approaches to introduce FEC (i.e., material and geometrically based) are considered, separately and together. To effectively determine the optimum design parameters in all the adopted control techniques, both normal operation and idling cases are considered within the optimization process.

The paper is structured as follows. Section 2 briefly describes the above-listed numerical tools and further details the optimization methodology followed. Section 3 presents and discusses the results of the various optimization analyses performed and, finally, Section 4 provides some overall conclusions comparing and assessing the different passive load control methods employed in the work.

2. Numerical Tools and Methodology

In the present section, the numerical tools constituting the multidisciplinary aeroelastic optimization framework used in the present work are briefly outlined. Relevant references, in which there are detailed description and validation of the models used by the optimization framework, are provided in the subsequent sections.

2.1. Multibody Servo-Aero-Elastic Analysis Tool hGAST

Nonlinear time domain aero-elastic simulations of the full wind turbine are performed using NTUA's in-house servo-aero-elastic hGAST [11,14,15]. The solver has been extensively used in numerous (national and EU-funded) research projects over the last 30 years, as well as by the industry. Its predictions for offshore applications have been verified through code-to-code comparison in the OC4 annex [19,20]. hGAST is formulated in the context of multibody method. The full wind turbine configuration is configured as an assembly of independent components, i.e., the blades, the drive train and the tower. The above components are modelled as linear Timoshenko beam elements, which are inter-connected through appropriate kinematic and dynamic constraint conditions. The multibody formulation is also extended to the component level. Highly flexible components, such as the wind turbine blades, are further divided into a number of rigidly interconnected "sub-bodies". Large deflections and rotations gradually build up and nonlinear dynamics are introduced by imposing to each sub-body the deflections and rotations of preceding sub-bodies as rigid-body nonlinear motions. This approach allows for capturing the geometrical nonlinear effects due to large deflections and rotations using linear beam theory at the element level, but considering nonlinear effects at the sub-body level.

Although several aerodynamic options are available in hGAST [15] (i.e., Blade Element Momentum Theory-BEMT, free wake vortex and finite volume CFD), in the present work, the BEMT approach is adopted, which is the only feasible in terms of computational cost for optimization analyses. The BEMT model used in hGAST is an elaborate version of the standard implementation in which dynamics inflow, yaw misalignment and sectional unsteady aerodynamics and dynamic stall effect are taken into account. Two stall models are available in hGAST, the ONERA [7] and the Beddoes–Leishman [6] model. A separate module that provides turbulent inflow boxes is also available, formulated on the basis of Veers' model [21]. For the calculation of the turbulent inflow wind time series either the von Karman or the Kaimal spectra, specified in the IEC 61400-1 standard, can be used.

2.2. Cross-Sectional Analysis Tool

An in-house cross-sectional analysis tool, based on thin lamination theory [16], is employed for the calculation of the distribution of shear stresses over the cross-sections of the different components of the wind turbine (e.g., blades and tower) as well as for the calculation of Tsai–Hill failure criterion [13]. The cross-sectional tool uses as input for the stress analyses, ultimate resultant loads with respect to a reference point on the cross-section, provided by the time domain aeroelastic analyses with hGAST. The same tool is also used for the calculation of the equivalent beam structural characteristics of the cross-sections, which become input to hGAST for the time domain aeroelastic analyses of the design load cases. It calculates equivalent beam inertia (e.g., mass and moments of inertia) and stiffness (e.g., bending and torsional) characteristics of hollow tubular sections with laminated composite skins and shear webs, while it is capable of treating the anisotropic behaviour of material plies (as shown in Figures 1 and 2). Therefore, it can provide fully populated stiffness matrices, taking into account all material-driven coupling effects and it can be used for the modelling of the FEC and BTC blades dealt with in the present work. In a recent upgrade of the model [10], the possibility to include up to three shear webs within a cross-section is added as an extra modelling feature (necessary for the modelling of the DTU-10 MW Reference blade, which comprises a third small TE shear web). In the same work, a more consistent computation of the shear rigidity properties is performed through the definition of appropriate Timoshenko shear factors, depending on the geometric characteristics in the section. The reader is directed to [10] for detailed description and verification of the cross-sectional tool.

2.3. Wind Turbine Cost Model

A cost model of the full wind turbine was set up by combining models from the literature that estimate the cost of the materials in the various components along with the cost of the manufacturing processes. The detailed cost model by NREL [22] is adopted for the blades, while the cost of the other parts of the rotor (i.e., hub, spinner and pitch mechanism) is based on empirical expressions provided in [23]. The cost estimation of the generator, the gearbox and the tower is derived through up-scaling [24] the data of a reference wind turbine of nominal power of 1.5 MW, which is described in detail in [23]. For detailed description and verification of the cost model, the reader is directed to [17].

2.4. Optimization Framework

The definition of the general optimization problem is:

Minimization of the objective function $f(\{v_S, v_A\}, \{c_S, c_A\})$ with design variables v_S, v_A and fixed parameters c_S, c_A, subject to the following geometric constraints.

$$g_A(v_A) \leq 0, \ g_S(v_S) \leq 0, \ g_{WT}(v_A, v_S) \leq 0 \tag{1}$$

and to the following loading constraints

$$\ell_S(v_A, v_S) \leq 0, \ \ell_{WT}(v_A, v_S) \leq 0 \tag{2}$$

The scalar objective function *f* is the *LCoE* of the entire turbine that requires as input the material distribution and mass of the turbine components as well as the annual energy production (*AEP*). The objective function depends on a number of structural design variables, v_S, (e.g., thickness of skin and webs, position and angle of the shear webs, fibre angle, etc.) and aerodynamic design variables, v_A, (e.g., chord, twist, relative thickness and sweep distributions), a set of fixed structural parameters, c_S, (e.g., lay-up sequence on different regions on the section) and aerodynamic parameters, c_A, (e.g., airfoil shapes and lift-drag polars selected from a database).

During the optimization loop, the following types of constraints are satisfied, as illustrated in Figure 3:

(i)   Geometric constraints that concern (a) the outer geometry of the blade and directly affect the aerodynamics, g_A, (e.g., maximum chord of the blade or maximum/minimum relative thickness), (b) the inner-blade structure, g_S, (e.g., maximum plausible displacement of the spar caps or the offset ply angle of the UD material over the spar caps) and, finally, (c) the overall turbine characteristics, g_{WT}, (e.g., maximum deflection of the blade tip or maximum shift of the blade natural frequencies).

(ii)   Loading constraints that are (a) maximum stresses, ℓ_S, along the blade and (b) overall turbine loads, ℓ_{WT}, as, for example, maximum rotor thrust or maximum blade root bending moment.
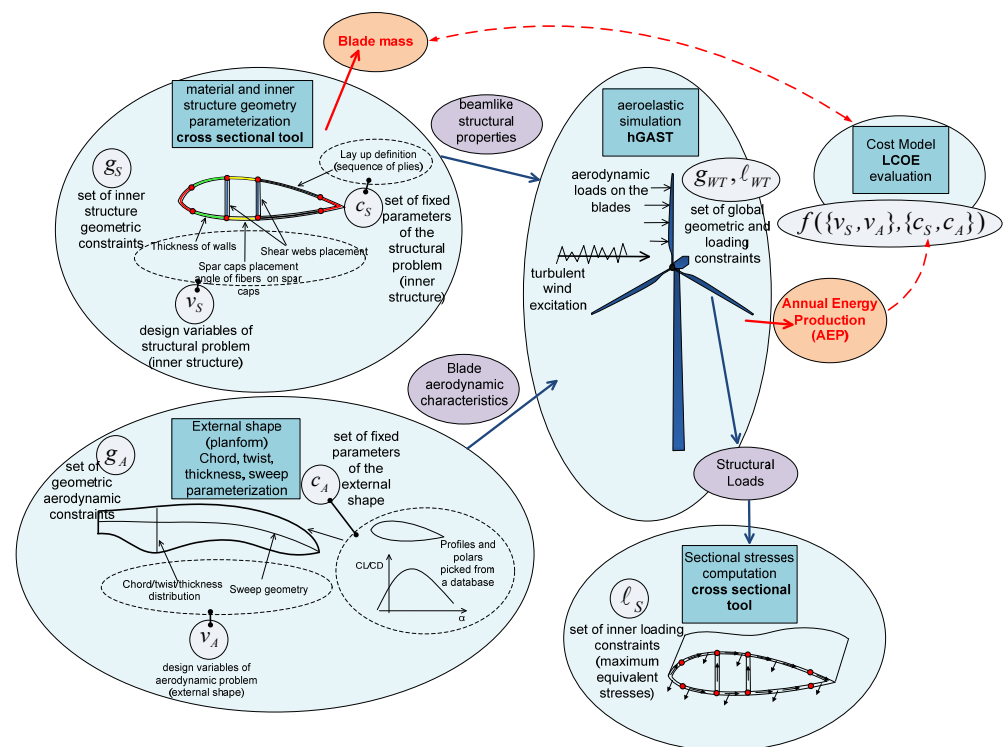

Figure 3. Overview of the optimization process.

Communication interfaces are established between the different modules in the optimization loop. An inner-structure geometry parameterization routine is integrated into the cross-sectional analysis tool. This routine is responsible for defining the inner shape of the blade through the global set of design and fixed variables v_S and c_S. A global, spanwise parameterization of the geometry is defined on the basis of Bezier curves for inner-structure parameters, such as the thickness of the skin walls or the position/orientation of the shear webs. A similar parameterization routine is defined for the representation of the external blade shape on the basis of v_A and c_A using Bezier curves.

In the present work, the objective of the optimization framework is to minimize the *LCoE* of the reference wind turbine through the optimal use of different passive load control

techniques (i.e., FEC and BTC) applied on the rotor blades. Apart from the rotor, the remaining wind turbine components remain unchanged, while only loading constraints concerning the maximum stresses along the blades are considered.

The *LCoE* is given by:

$$LCoE = \frac{\overbrace{(ICC + BoP)}^{CAPEX}\frac{i}{1-(1+i)^{-N}} + OPEX}{AEP} \tag{3}$$

where *ICC* is the initial capital cost provided by the cost model, *BoP* is a global approximation of the balance of plant, considered equal to 281 USD/kW of installed capacity, *OPEX* denotes the operating expenses, considered equal to 5% of *ICC* and *AEP* is the annual energy production, calculated by the aeroelastic tool. The *LCoE* in the present analyses is calculated for a life-time of the investment of $N = 20$ years and a discount rate of $i = 6\%$.

The *AEP* is calculated through a series of time domain aeroelastic simulations with hGAST (see Section 2.1) over the whole range of the operating wind velocities (from the cut in to the cut out). Additional time domain simulations of selected load-driving DLCs of the IEC standard, including both normal operation and parked-idling operation cases, provide ultimate design loads for the candidate optimum solutions. The ultimate loads are then transformed to stresses and Tsai–Hill criterion values (equivalent stresses) by the thin lamination tool (see Section 2.2) over the cross-sections in every component (e.g., blade and tower). The imposed constraint to the optimization process requires that the Tsai–Hill criterion values do not exceed the corresponding values of the reference blade. In this way, the thickness of the component walls and the design parameters of the passive load control methods tested by the optimizer are determined. Knowing the dimensions and the material distribution in the load carrying elements of the components the overall capital expenditure (CAPEX) of the candidate solution can be estimated using the cost model (see Section 2.3).

The minimization problem is addressed through the free-gradient optimizer 'COBYLA', which is publicly available as Python module of the scipy library [18] and is divided into two loops with the aim to moderate the computational cost of the optimization loop [10,12]. The outer loop specifies the parameters of FEC and BTC. In the present work, this includes the definition (i) of the thickness distribution along the blade span of the L/P "leading" and H/P "trailing" segments of the cross-sections in the material FEC method (see Figure 1, left), (ii) of the displacement of the caps in the geometrical FEC method (see Figure 1, right) and (iii) of the ply offset angle of the material BTC blades (see Figure 2). Furthermore, the outer loop adjusts the geometric characteristics of the blade (blade planform, i.e., the twist angle distribution) and evaluates the cost function (*LCoE*). The inner loop specifies an overall, uniform thickness coefficient for the walls of every cross-section that varies along the span. Its purpose is to estimate the thickness of the blade walls in such a way as to maintain the maximum values of Tsai–Hill criterion of the reference blade (constraint of the optimization process). This part of the optimization process is the most time consuming because it includes the computation of the ultimate resultant loads with hGAST, as well as the calculation of the beam properties and stress distributions of the modified blades based on the FEC and BTC with the cross-sectional tool.

2.5. Methodology

In this section, the different optimization scenarios addressed in the present work are detailed, while further specific information concerning the simulations performed for the assessment of candidate optimum solutions is provided.

In Table 1, the five optimization cases (CASE A, B, C, D and E) examined in the paper are listed along with the passive control designs applied.

Table 1. DTU-10MW RWT passive control designs aimed at minimizing the *LCoE*.

Design	FEC Material	FEC Geometrical	Re-Twist	BTC	Comments
Reference					DTU-10MW RWT
CASE A	√				FEC control
CASE B		√			FEC control
CASE C	√	√			FEC control
CASE D	√	√	√		FEC with re-twist
CASE E	√	√	√	√	FEC&BTC with re-twist

CASE A, concerns material FEC which is based on the thickening of the L/P "leading" and the H/P "trailing" element of the cross-section walls, respectively (see Figure 1, left). In this optimization study, a different coefficient for the wall thickness increase is applied to each element that varies along the span of the blade. The radial distributions in the two coefficients (i.e., for the L/P and H/P sides) are parameterized using global Bezier interpolation functions with three control points (CP) per distribution. In the optimization process, three parameters per distribution (six in total) are considered as design variables: (i) the value of the coefficient of the first CP, which is fixed at the blade root, (ii) the value of the coefficient of the second CP and (iii) its radial position. The third CP is considered fixed at the blade tip with a fixed value of one (i.e., no thickness change is performed). In addition to the above two coefficients applied to specific segments of the cross-section, a global thickness coefficient is also considered for all the elements in the cross-section. It varies radially, in a discrete manner at the 21 radial sections analysed. In CASE A the planform of the blade is considered fixed and identical to that of the reference blade.

CASE B concerns geometric FEC which is based on the displacement of the spar caps of the two sides of the cross-section in opposite directions (see Figure 1, right). In this case study, a different percentage shifting (relative to the section chord length) of every cap is considered that varies along the span of the blade. The radial distributions of the percentage displacements (for the L/P and H/P sides) are parameterized using again global Bezier interpolation functions with three CPs. As previously, the same three parameters in each distribution are considered as design variables and the remaining three parameters are kept fixed. Further, a global thickness coefficient is applied to all the elements in the cross-section at 21 radial stations while the planform of the blade is considered fixed.

CASE C concerns the combined application of both the above two methods. It is sought whether a combination of the two methods could be more flexible in tailoring the structural twist angle distribution. In order to reduce the total number of design variables (of the combined application of the two methods) from 12 to 8, the radial positions of the intermediate (mid-span) Bezier CPs of all curves are maintained fixed to the positions that simulations of CASES A and B converged to. The above choice implies that the overall shapes of the radial distribution curves would be quite insensitive to the exact radial placement of the intermediate CP.

CASE D concerns the combined application of both the above two methods (i.e., CASE C) in conjunction with the redesign of the blade twist. As mentioned in the introduction section, FEC entails an indirect, unfavourable BTC effect, induced by the forward sweep deflection. The above BTC effect causes a nose-up twisting of the blade sections that gives rise to increased flapwise loads. Re-twisting of the blade could be a means to mitigate the above effect. The twist distribution of the blade is parameterized using global Bezier interpolation functions with three CPs. The radial position and the twist of the first CP are fixed at $r/R = 0.15$ and $\theta_{twist} = -13.1°$. The radial position of the second and the third CP are fixed at $r/R = 0.25$ and 1, respectively, while the twist angle of these CPs is considered as a design variable.

CASE E concerns the combined application of both the above two methods (i.e., CASE D) in conjunction with material BTC (application of offset angle θ to the UD plies over the

spar caps, see Figure 2). As discussed in the introduction section, the aim of BTC in this case is to alleviate any negative effects of FEC on operational loads. BTC begins at r/R = 0.2 and consists of only one design variable (a constant ply offset angle which is applied from r/R = 0.2 up to the blade tip). The mechanism through which BTC alleviates loads is the nose-down twist rotation that takes place whenever the blade is subjected to excessive flapwise deflections, acting as a passive control of the flapwise loads of the blade [11]. The induced torsional deformation due to BTC suggests that effective optimization of the loading and of the performance requires a redesign of the blade aerodynamic twist. The same parameterization of the blade twist distribution, as well as of the FEC parameters is employed as in CASE D.

As discussed in Section 2.4, a subset of the most critical DLCs of IEC 61400-1 are simulated within the inner-optimization loop using hGAST, in order to determine the design loads of the components. In terms of normal operation conditions, simulations of DLC-1.3 (extreme turbulence wind conditions in normal operation) at a wind speed of 13 m/s are performed. Earlier studies showed [10] that the above DLC is the design-driving DLC for the ultimate loads of the reference rotor. It is important to note that rationalization of the computational cost is absolutely critical at this point. To this end, the duration of the normal operation time domain simulation is limited to 50 s. The simulation window is centred on the time instant for which maximum loads of the reference rotor in a simulation with a total duration of 30 min are obtained for most of the cross-sections. It is noted that even for the cross-sections where maximum load occurs at a different time instant, still the load within the selected window is very close to its maximum. The above choice, dictated by the requirement for affordable computer cost, does not ensure that ultimate load is always tracked down. However, previous studies [10] indicated that following the above approach, loads do not significantly deviate from the actual ultimate loads. Besides, optimized designs are eventually verified on the basis of detailed turbulent wind simulations over a range of wind and operation conditions, as demonstrated in Section 3.4. As far as idling operation is concerned, the simulations of DLC-6.2 (turbine set in idling mode during the occurrence of 50-year return period wind speed and a grid loss) are at a yaw angle of 30° and at a wind speed of 50 m/s (50-year return period wind speed for the class IA, DTU 10 MW reference turbine). A larger time window of 300 s is considered for the idling turbine simulations, given that the uncertainty of the prediction of the ultimate load in idling mode is significantly higher compared to the one in normal operation mode. This is especially true in the event of flutter instability.

Within the inner-optimization loop, design of the inner structure wall thickness is performed under the constraint that the maximum values for the Tsai–Hill criterion in every cross-section of the reference blade (only due to normal operation extreme loads) are not exceeded. It is noted that the above constraint is rather conservative compared to the requirement that Tsai–Hill criterion values should remain below the failure limit of one. The reason is that, in this way we neglect any possibility that the reference blade may be overdesigned. This could be the explanation of why its Tsai–Hill values are lower than the failure threshold. It is also noted that in the present study, equivalent stress constraints are only applied to the blade loads. Optimization of the tower is out of the scope of the present study. However, in the final assessment of the optimum designs for the three case studies considered, it is showcased that eventually the designed interventions performed on the blades do not harm tower loads.

3. Results and Discussion

3.1. Ultimate Load Assessment of the DTU-10MW RWT

In the present section, the design loads of the baseline DTU 10MW RWT are estimated. A subset of the most critical ultimate DLCs of the IEC 61400-1 standard for class IA (the design class of the reference turbine) are simulated using hGAST. The test matrix for the simulated DLCs is provided in Table 2. DLC-1.3 corresponds to extreme turbulence conditions (ETM) and determines the ultimate limit state (ULS) for normal operation

(most critical normal operation DLC). Simulations are performed for wind speeds in a range (9–25 m/s) with a step of 4 m/s. DLCs-6.x is chosen as the most unfavourable, non-operating DLC (idling operation at the survival wind speed with 50-year recurrence period). Simulations are performed at a wind speed of 50 m/s for various yaw misalignment angles in a range of (−60°, 60°). Moderate yaw angles in a range (−15°, 15°) are considered in DLC-6.1 (normal idling operation), while higher yaw angles outside the above range are considered in DLC-6.2 (idling operation combined with loss of grid). Three wind seeds (of 10 min duration each) are simulated in every test case.

Table 2. DLC definition for ultimate load assessment.

DLC	Conditions	Wind Speeds [m/s]	Yaw Angle [deg]	Safety Factor [−]
1.3	ETM	9–25, step 4	0	1.35
6.1	EWM	50	0	1.35
6.2	EWM	50	±15, ±30, ±45, ±60	1.10

The design loads of the DTU 10MW RWT are presented in Figure 4. The plots depict, separately, the ultimate combined blade root and tower moments for the analysed cases. Safety factors are applied to all loads based on the specifications of the IEC 61400-1 standard (see [2]). All simulations are performed using the Beddoes–Leishman dynamic stall model. As seen in the figure, maximum blade and tower loads are obtained at a yaw angle of 30°. More specifically, the blade moment exhibits an increase of almost 40% at a yaw angle of 30°, in relation to the loads of the neighbouring yaw angles of 15° and 45°. An increase in blade loads is also noted at a yaw angle of −30°; however, this appears to be much lower. The abrupt increase in the blade loads at 30° yaw is due to stall-induced vibrations at the frequencies of the rotor edgewise asymmetric modes. It is important to note that when idling operation simulations are performed using the ONERA dynamic stall model (the corresponding results are not shown in Figure 4), substantially lower ultimate loads are obtained at a yaw angle of 30°. Predictions of the two models notably deviate only at this particular yaw angle, i.e., at the onset of the stall flutter, while similar load predictions are obtained by the two models in the operational case. This notable difference in the two models around the onset of the instability leads to the following mismatch: when the Beddoes–Leishman model is employed, the design-driving DLC is 6.2 at +30° yaw, while when the ONERA model is used, DLC-1.3 at 13 m/s wind speed determines the design load. Given that it is by no means straightforward to conclude which of the two models is more accurate, the best way to bypass this uncertainty is by suppressing the obtained instabilities through the passive increase in the damping of the low-damped rotor edgewise modes.
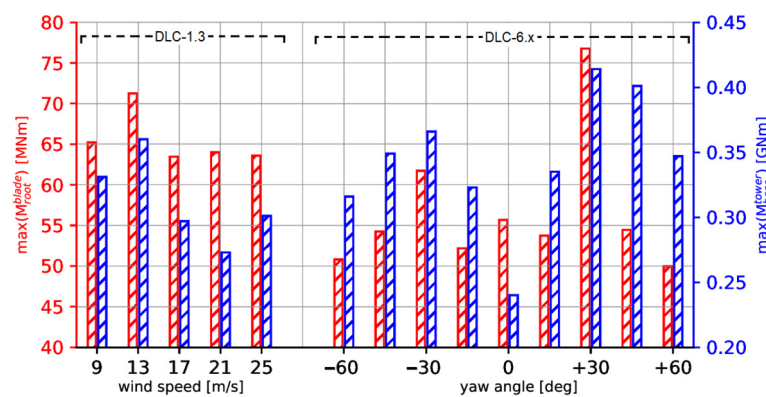

Figure 4. Maximum combined bending moment at blade root (red bars) and tower base (blue bars), for DLC-1.3 and DLC-6.x, for various wind speeds and wind yaw angles.

3.2. Material and Geometric FECCASES A and B

The optimization results of CASES A and B are presented in this section. In those two scenarios, the two FEC methods for the suppression of stall-induced vibrations are implemented and assessed separately, one from the other.

In Figure 5, the optimum values of the six design variables (v_1–v_6) of CASE A (material FEC) that define the radial distribution of the thickness increase coefficients in the walls of the L/P "leading" and H/P "trailing" elements are presented along with the corresponding Bezier curves. In the same figure, the global thickness variation coefficient of all the walls is also shown. As seen in the figure, a higher increase in the thickness is required for the "leading" element, all along the blade span. At the root of the blade, the thickness increase coefficient is equal to 5.5 for the "leading" element and 3.3 for the "trailing" one. This high increase in the thickness of the two elements is accompanied by a global reduction coefficient for the thickness of all walls of about 0.5. Beyond r/R = 0.3, the global thickness coefficient returns to values slightly lower than 1, while the thickness increase coefficient for the "leading" element still obtains high values (close to 5) that gradually decrease towards the blade tip. The thickness increase coefficient for the "trailing" element, beyond r/R = 0.3, drops to values close to 1. Application of material FEC reduces blade mass by 10.3% and overall *LCoE* by 0.82%. A marginal increase in *AEP* of 0.12% is also obtained, which is due to the indirect twisting effect caused by FEC in normal operation. The virtual forward sweeping of the blade due to FEC causes nose-up twisting of the blade sections, which leads to slightly higher power output of the blade.
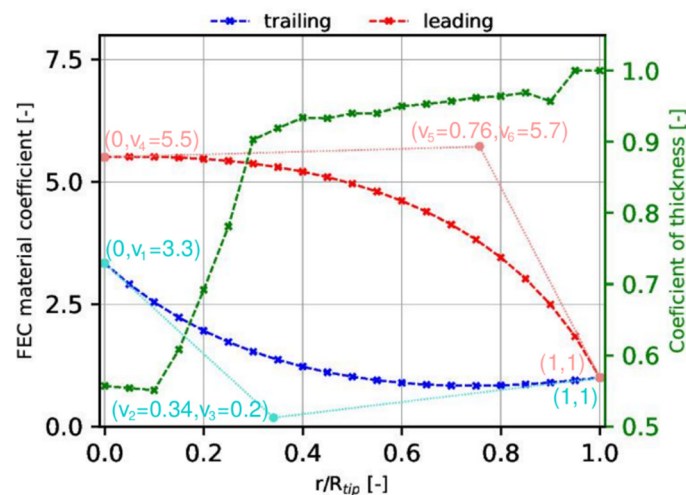

Figure 5. Material FEC (CASE A): coefficients of change in thickness of the materials 'TRIAX' and 'UNIAX', for the regions H/P "trailing" and L/P "leading" and global coefficient of the cross-section thickness (with green color). Cyan and orange symbols depict control points, connected with straight lines.

In Figure 6, the optimum values of the six design variables (v_7–v_{12}) of CASE B (geometric FEC) that define the radial distribution of the shift in the spar caps are presented along with the corresponding Bezier curves. The positive shift is the one towards the trailing edge (TE). In the same figure, the global thickness variation coefficient for all the walls is also shown. As seen in the figure, the L/P cap is shifted towards the leading edge by 10.4% at the blade root, while the displacement of the H/P cap is somewhat lower (7.2%) and it is towards the TE. The displacement of the L/P cap decreases towards zero with the increase in the radial position. Some small positive displacements in the order of 1% are noted for radial positions higher than 0.5. It is important to point out that the effect on the cross-bending stiffness is obtained as a result of the relative motion of the two caps and not as a result of their absolute position per se. This can be seen in Figure 6, where, although for r/R > 0.5, the L/P cap moves towards the TE, its relative displacement with respect to

the H/P cap remains in the same direction. The displacement of the H/P cap remains high (7–10%) up to the radial station r/R = 0.5 and thereafter, drops towards zero.
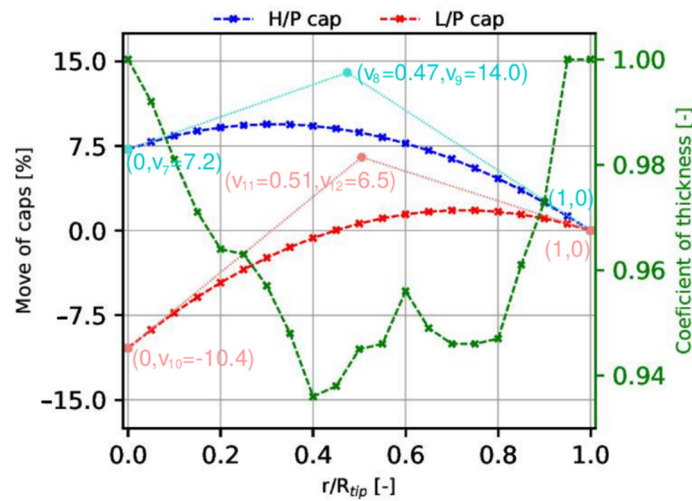

Figure 6. Geometric FEC (CASE B): span-wise distributions of percentage shift in the caps relative to the chord and global coefficient for the cross-section thickness (with green color). Cyan and orange symbols depict control points, connected with straight lines.

A notable difference between the two methods is that while the material FEC attains the increase in cross-bending stiffness by intervening on the thickness of the L/P side (L/P "leading element), in the geometric FEC, the increase in the cross-bending stiffness is mainly achieved by the backwards displacement of the H/P cap. Therefore, it is a result of an intervention mainly on the H/P side. It should also be noted that the global thickness coefficient in the geometric FEC method remains close to 1 all along the blade span (minimum value ~0.94). Application of the geometric FEC reduces mass by 3.1% and *LCoE* by 0.36% (substantially lower reductions than those for the material FEC). Similar to CASE A, a marginal increase in *AEP* of 0.18% is also obtained, as shown in Figure 7.
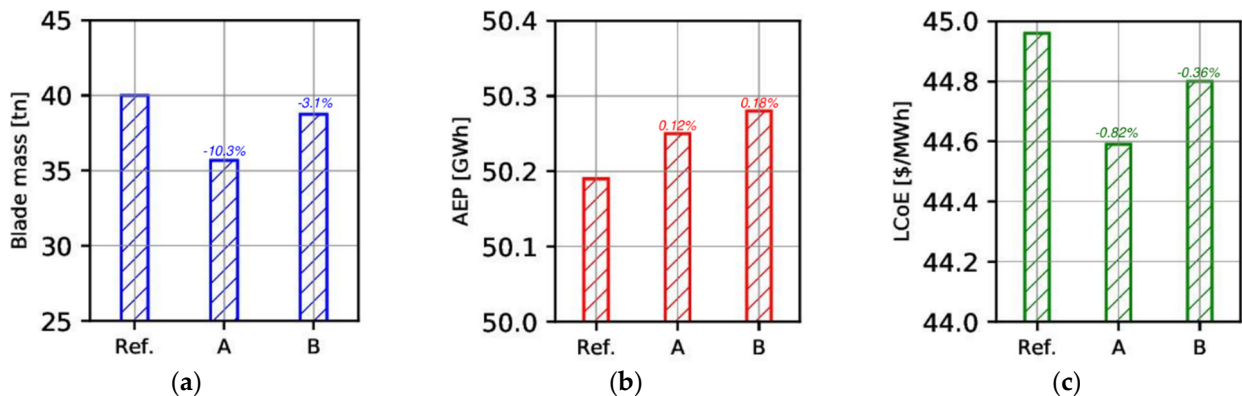

Figure 7. (**a**) Blade mass, (**b**) annual energy production and (**c**) Levelized Cost of Energy, of the material FEC (CASE A) and the geometric FEC (CASE B) designs and relative percentage differences with respect to the reference configuration.

In Figure 8, the structural twist distribution (see definition of structural twist in [10]) of CASES A and B is depicted (along with all other configurations analysed in the next section). It is seen that material FEC gives rise to a high local increase in the structural twist to feather direction (negative twist values) in a radial range of 0.1–0.2. On the other hand, geometric FEC causes an almost constant and much smaller shift in the structural twist all along the span. The positive structural twist angles at the innermost sections (r/R < 0.1)

do not affect the stability characteristics of the blade. They are obtained as a result of the redistribution by the optimizer of the material over the root sections in a way that loads are supported. The minor effect of the geometric FEC on the structural twist justifies its limited capability to reduce blade mass and *LCoE*.
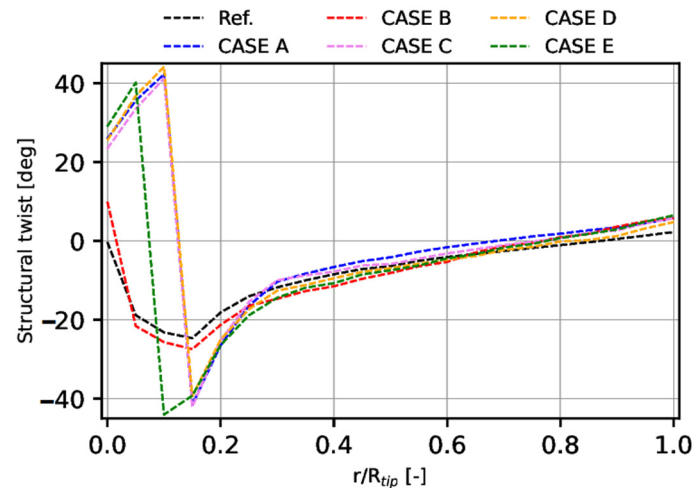

Figure 8. Structural twist distribution of the design configurations.

3.3. Combined Application of Passive Control Methods—CASES C, D and E

In the present section, CASES C, D and E, in which combined application of different passive load control methods is performed, are addressed.

In CASE C, combined application of the two FEC methods (material and geometric) is performed. Figures 9 and 10 provide the radial distributions of the material thickness coefficients and of the caps' displacement, respectively, for CASE C and all other configurations analysed. It is seen that the combined application of the two methods does not significantly alter the design parameters of the material FEC. On the other hand, the radial distributions of the caps' displacement appear to be much more sensitive (see Figure 10). This is justified by the observation made in Section 3.2 that the material FEC is far more effective in adjusting the structural twist. Thus, while the predominant design variable that affects structural twist exhibits similar behaviour with that of CASE A, the secondary parameter, which only has an additive effect, is let free by the optimizer to vary a lot more (i.e., the optimum is rather flat). It is interesting to note that, in particular in CASE C, the optimizer finds that the optimum displacement for the H/P cap is towards the LE, while the L/P cap remains almost un-displaced. Although this seems to be a paradox on first reading, it is explained by the fact that moving the H/P cap towards the leading edge leads to an increase in the H/P "trailing" element, leaving more space for material FEC to adjust the cross-bending stiffness. The reduction in the mass achieved by CASE C is 13.3%, which is, more or less, the summation of the reductions achieved in CASES A and B. The reduction in the *LCoE* in CASE C is 1.02%, slightly lower than the sum of the reductions attained in CASE A and CASE B. Similar to CASES A and B, a very small increase in *AEP* of 0.16% is obtained.

In CASE D, the re-twist of the blade acts as an additional mechanism for adjusting structural twist. As seen in Figure 8, the structural twist distribution of CASE D configuration resembles that of CASE A. This means that, as in CASE C, the structural twist distribution is dictated by material FEC. Further, the re-twisting of the blade at its tip towards the feather direction, as shown in Figure 11, enhances the cross-bending stiffness at the tip region of the blade. As in CASE C, the thickness coefficients of material FEC are similar to those of CASE A and C (see Figure 9). Slightly smaller thickness increase coefficients are noted for the H/P "leading" element, which are compensated by the slightly higher displacement of the H/P cap towards the LE, as compared to CASE C (see Figure 10). CASE D has an incremental effect on mass reduction as compared to CASE C (14% mass

reduction vs. 13.3% for CASE C) and it has a neutral effect on *LCoE* (reduction of 1.02% as in CASE C). As in all previous cases, a marginal increase in *AEP* of 0.14% is noted.
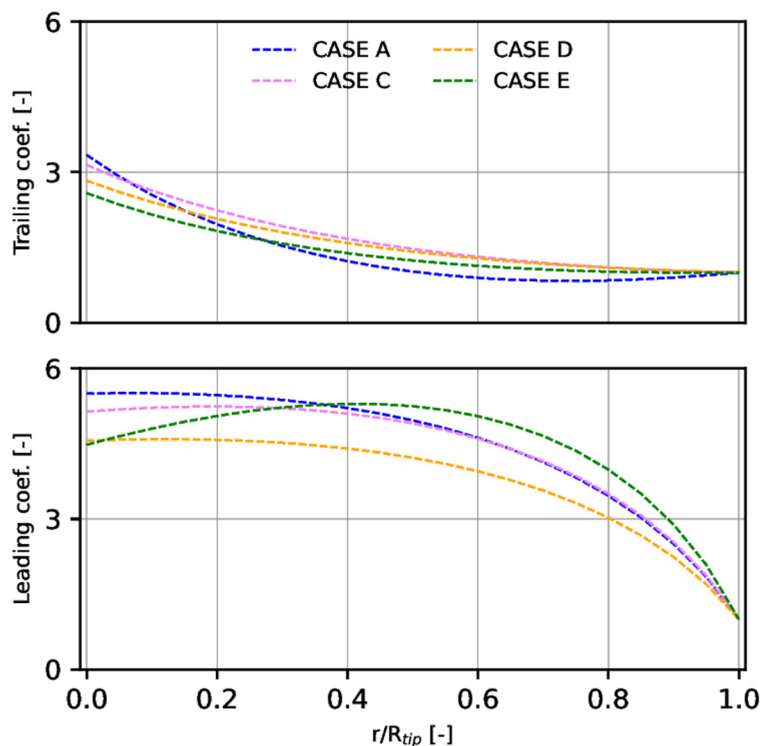
Figure 9. Distribution of the material FEC coefficient for the leading (**top**) and trailing (**bottom**) region of the cases: A, C, D and E.
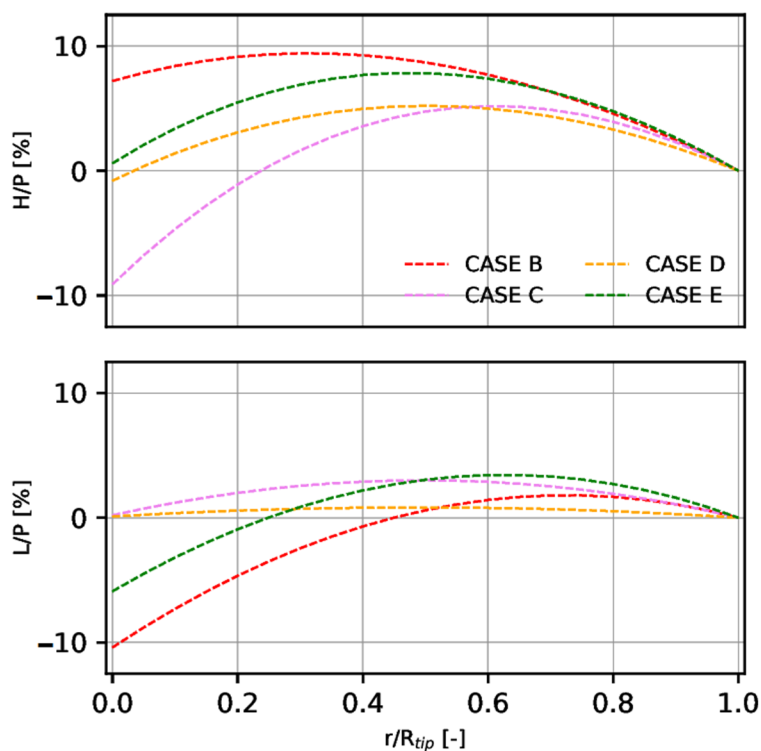
Figure 10. Distribution of the geometric FEC coefficient for the high-pressure (**top**) and low-pressure (**bottom**) cap of the cases: B, C, D and E.
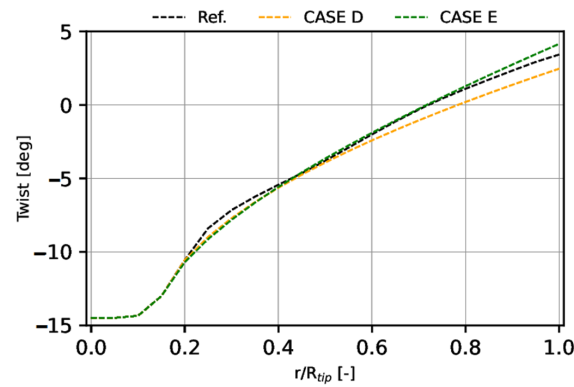
Figure 11. Twist distribution of the cases: reference (A–C), D and E.

The results of CASE E, in which all interventions are combined together, are summarized in Figure 12. The figure provides the optimum distributions of the design parameters in the passive control modifications considered. The optimum ply offset angle obtained by the optimizer is 6.2°, as shown in Figure 12d, being totally aligned with previous studies [11,12,17]. Furthermore, BTC allows for much higher global sectional thickness reduction coefficients as compared to CASES A and B. As seen in Figure 12d, the average value of the global thickness coefficient is ~0.75. The result of the blade re-twisting is a twist to feather at the inner part of the blade and a twist to stall at the tip region (see Figures 11 and 12c). The aim of the first is to increase the structural twist at the inboard sections. The aim of the latter is to compensate the twisting of the blade towards the tip due to the BTC effect. As in CASES C and D, the structural twist distribution is dictated by the material FEC (see Figure 8). Moreover, the distributions of the thickness coefficients of the material FEC are very similar to those of all previous cases (see Figures 9 and 12a). As opposed to CASES C and D, a notable shift in the L/P cap towards the LE is obtained in this case (−5.9% at the root of the blade), while the displacement distribution of the H/P cap is very similar to the one in CASE D (see Figure 12b).
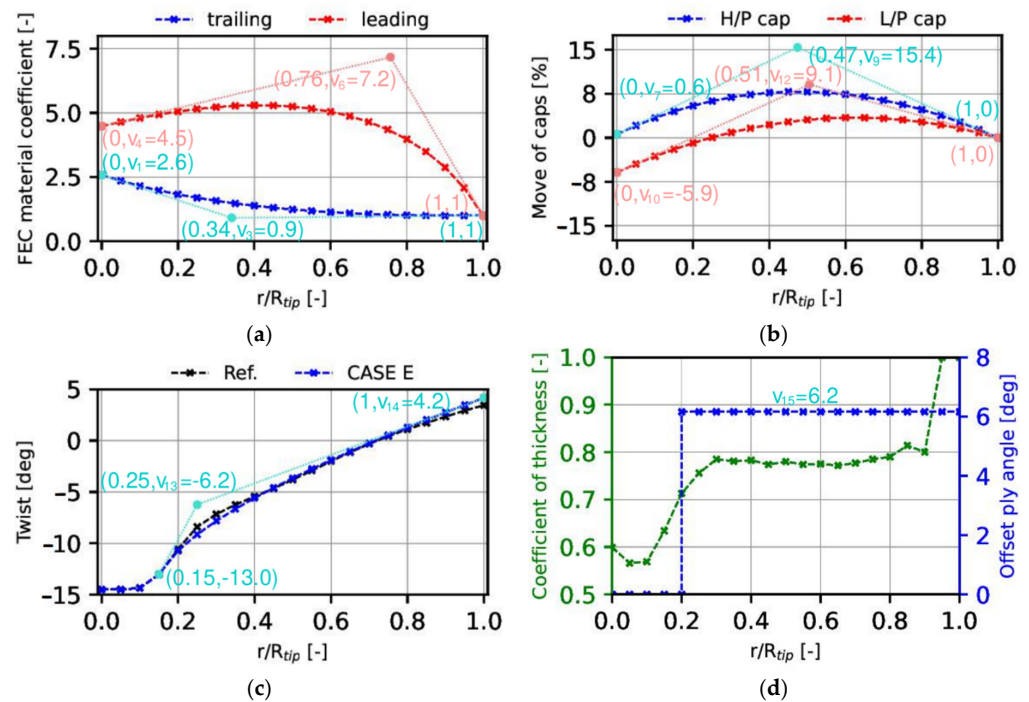

Figure 12. CASE E: distribution of (**a**) FEC material approach, (**b**) FEC geometrical approach, (**c**) twist and (**d**) offset ply angle of 'UNIAX' material and coefficient of wall thickness.

CASE E has a substantial additional mass reduction effect as compared to CASE D (19.5% vs. 14% of CASE D), which is obviously due to the application of the BTC. The *LCoE* reduction in CASE E is 1.36%, the highest of all studied cases. Again, a marginal increase in *AEP* of 0.16% is attained. Figure 13 summarizes the optimum value of the blade mass, *AEP* and *LCoE*, obtained with the MDAO process for the considered designs (CASES A–E). For the sake of completeness, all designs are shown in the figure, including CASES A and B that have already been presented in Figure 7.
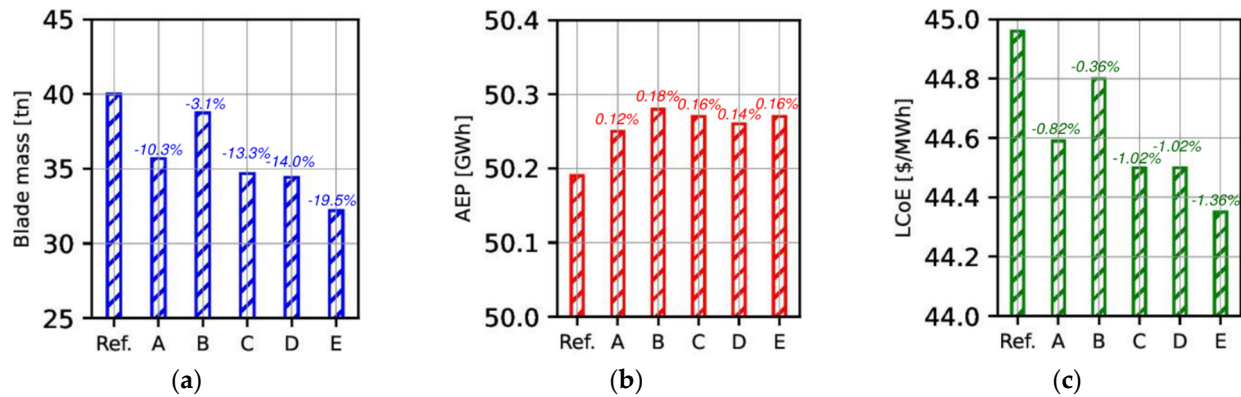

Figure 13. (**a**) Blade mass, (**b**) annual energy production and (**c**) levelized cost of energy of the different designs and relative percentage differences with respect to the reference configuration.

Finally, Table 3 details the design variables considered per design (CASES A–E). In the table, the optimum value per design variable is provided for all the cases considered. The horizontal lines are introduced to distinguish the various design interventions performed, i.e., the material FEC, the geometric FEC, the re-twist and the material BTC.

Table 3. Results for the design variables of the considered configurations. Numbers in red correspond to design variable values that remain fixed in the simulation.

	CASE A	CASE B	CASE C	CASE D	CASE E
v_1 (trailing.root CP in y-axis)	3.34	-	3.14	2.83	2.58
v_2 (trailing/interm. CP in x-axis)	0.34	-	0.34	0.34	0.34
v_3 (trailing/interm. CP in y-axis)	0.18	-	1.18	1.18	0.91
v_4 (leading/root CP in y-axis)	5.50	-	5.14	4.56	4.48
v_5 (leading/interm. CP in x-axis)	0.76	-	0.76	0.76	0.76
v_6 (leading/interm. CP in y-axis)	5.73	-	5.90	4.92	7.17
v_7 (H/P cap/root CP in y-axis)	-	7.20	−9.10	−0.80	0.60
v_8 (H/P cap/interm. CP in x-axis)	-	0.47	0.47	0.47	0.47
v_9 (H/P cap/interm. CP in y-axis)	-	14.00	13.80	10.80	15.40
v_{10} (L/P cap/root CP in y-axis)	-	−10.40	0.20	0.10	−5.90
v_{11} (L/P cap/interm. CP in x-axis)	-	0.51	0.51	0.51	0.51
v_{12} (L/P cap/interm. CP in y-axis)	-	6.50	5.90	1.60	9.10
v_{13} (twist/interm. CP in y-axis)	-	-	-	−5.54	−6.24
v_{14} (twist/tip CP)	-	-	-	2.47	4.16
v_{15} (BTC angle)	-	-	-	-	6.16
Number of design variables	6	6	8	10	11

3.4. Assessment of Optimum Designs

In the present section, verification of the optimum designs A, B and E, from Sections 3.2 and 3.3, is performed. The strength characteristics of the optimum, tailored turbines are verified through detailed, time domain aeroelastic simulations of a selected subset of ultimate load cases for the IEC 61400-1 standard (see Section 3.1, Table 2), simulated using hGAST. The blade and tower loads in the tailored, optimized configurations are compared against those of the reference wind turbine. The aim of the verification step

is to perform a thorough check of the final optimum designs (the two FEC configurations and the configuration that combines all design interventions), which consists of a more extended list of DLCs and conditions and wider evaluation windows (in terms of simulated time series lengths) compared to those considered within the optimization loop.

Before assessing the loads in the different designs, a comparison of the natural frequencies of the variants A, B and E with the reference turbine is performed in Table 4, in order to identify possible critical changes in the dynamic characteristics of the new designs. As a result of the increased structural coupling in the flapwise and edgewise directions and the material re-distribution over the cross-sections, the frequencies of the rotor bending modes drop (both the flapwise and edgewise). Higher reductions, in the order of 8–9%, are noted in the frequencies of the asymmetric edgewise modes, in the application of material FEC. The maximum frequency reduction in the flapwise modes is in the order of 3.5–4% and it is, again, obtained for configuration A (material FEC). On the other hand, geometric FEC entails a lower reduction in the natural frequencies. Finally, the reduction in the frequencies noted in CASE E is similar to that in CASE A, most probably dictated by the material FEC. A slight increase is noted in the frequencies of the tower modes as a result of the lower-rotor mass achieved by all tailored designs. The frequency comparisons in Table 4 indicate that the performed structural modifications are not expected to significantly alter the overall dynamic behaviour of the coupled wind turbine system.

Table 4. Standstill natural frequencies of the reference DTU-10MW RWT and FEC designs. Relative percentage differences with respect to the reference configuration are also provided.

	Modeshape	Reference	CASE A	CASE B	CASE E
1	1st tower bending side-side	0.250	*0.8%*	*0.4%*	*2.0%*
2	1st tower bending fore-aft	0.253	*0.8%*	*0.4%*	*1.6%*
3	1st symmetric rotor edge/drive-train	0.521	*−3.5%*	*−0.4%*	*0.8%*
4	1st asymmetric rotor flapwise (yaw)	0.550	*−3.3%*	*−1.8%*	*−2.0%*
5	1st asymmetric rotor flapwise (tilt)	0.595	*−3.9%*	*−2.7%*	*−3.9%*
6	1st symmetric rotor flapwise	0.651	*−2.0%*	*−1.1%*	*−1.4%*
7	1st asymmetric edgewise (ver.)	0.969	*−9.1%*	*−0.8%*	*−5.7%*
8	1st asymmetric rotor edgewise (hor.)	0.982	*−8.5%*	*0.1%*	*−5.0%*

In Figures 14 and 15, the ultimate loads of the blades and the tower of the three turbine configurations (A, B and E) are presented as a function of the wind speed for DLC-1.3 and as a function of the yaw angle for DLC-6.1 and 6.2. The first important observation in Figure 15a is that the ultimate blade load of DLCs-6.x (yaw angle of 30°) is effectively reduced in all configurations. A maximum reduction of 25.8% is achieved for configuration E. A similar reduction is achieved with configuration A (25.6%), while a reduction of 19.5% is obtained for configuration B. In fact, the ultimate loads of DLCs-6.x even drop below the ultimate load of DLC-1.3 (obtained at a wind speed of 13 m/s) in all optimized designs. The suppression of stall-induced vibrations in the rotor edgewise modes in idling operation indirectly affects tower loads (see Figure 15b). The ultimate tower load decreases by 4.6% in configurations A and B and by 8.2% in configuration E. Furthermore, the optimized application of FEC, as well as the combined application of FEC and BTC, does not incur any increase in the blade loads in normal operation. As seen in Figure 14a, ultimate blade loads of all configurations are lower than those of the reference blade. Tower normal operation loads are also moderated, except for those in configuration B, for which a slight increase of 0.6% is noted in the maximum normal operation load while an increase up to 2.9% is seen at a wind speed of 21 m/s (see Figure 14b). However, it should be stressed that normal operation tower loads are far less than idling operation tower loads. DLC-6.2 is definitely the design-driving load case, both before and after the structural and aerodynamic interventions performed in the present study.
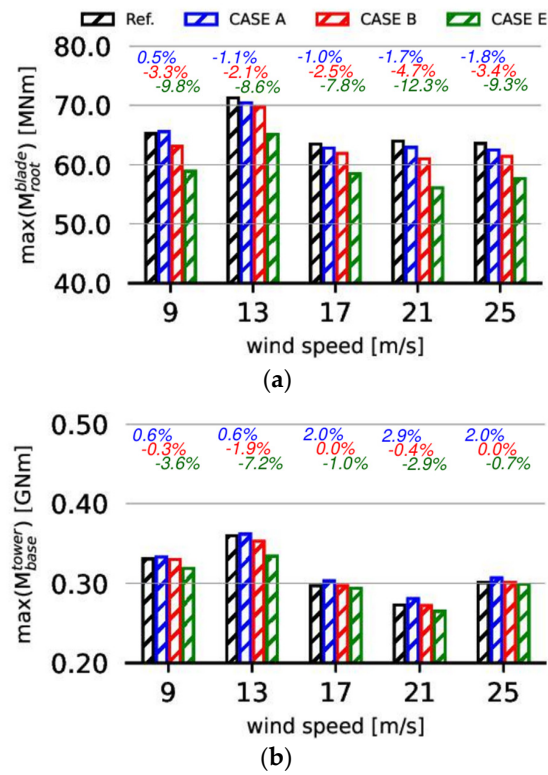
Figure 14. DLC-1.3 ultimate loads vs. wind speed of examined configurations (including safety factors) maximum combined bending moment (**a**) at the blade root and (**b**) at the tower base.
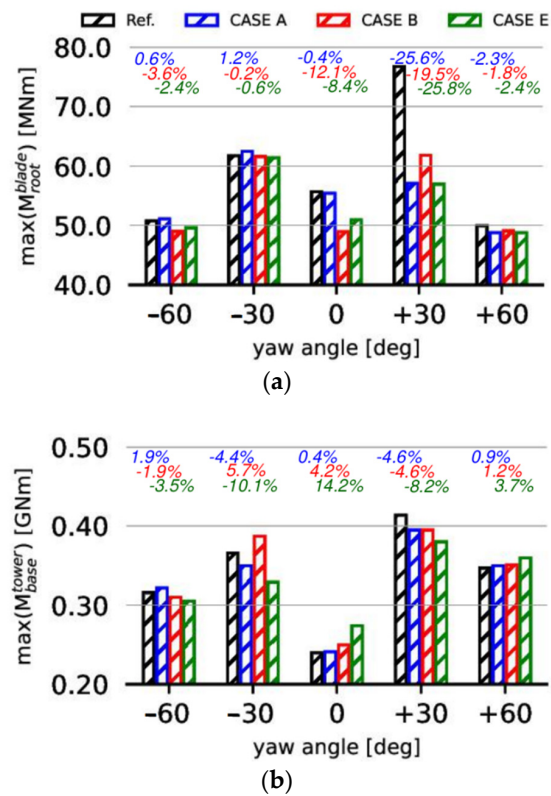

Figure 15. DLC-6.x ultimate loads vs. yaw angle of examined configurations (including safety factors) maximum combined bending moment (**a**) at the blade root and (**b**) at the tower base.

4. Conclusions

Design modifications of the blade inner structure, which lead to suppression of stall-induced edgewise vibrations in idling operation and, therefore, reduce design-driving loads, were assessed in this paper. The design parameters in two FEC methods (material and geometric) were optimized within an MDAO optimization framework, with the aim to minimize *LCoE*. Optimizations were performed based on a stepwise approach, in which the two FEC methods were first evaluated separately, then in combination and, finally, they were blended with material BTC and re-twist of the blade. Optimization studies indicated that material FEC, which is based on the asymmetrical increase in the thickness of the walls of the L/P side towards the section nose and of the H/P side towards the TE, is more effective in suppressing stall-induced instabilities and reducing *LCoE* than the geometric FEC, which is based on the displacements of the spar caps of the L/P and H/P sides in opposite directions. Geometric FEC leads to an almost constant shift in the structural twist angle all along the blade span, while material FEC results in a high local increase in the cross-bending stiffness and the corresponding structural twist angle in the inboard part of the blade. The latter turns out to give a mass reduction in the blade of 10.3% and a corresponding decrease in *LCoE* of 0.82%, while the former gives rise to a reduction in mass of 3.1% and of *LCoE* of 0.36%. Combined application of the two methods appears to have an accumulative effect, while additional application of BTC with a parallel re-twisting of the blade provides a maximum reduction in mass and *LCoE* of 19.5% and 1.36%, respectively.

References

1. Wang, K.; Riziotis, V.; Voutsinas, S. Aeroelastic stability of idling wind turbines. *Wind. Energy Sci.* **2017**, *2*, 415–437. [CrossRef]
2. *IEC 61400-1 Ed. 3*; Wind Energy Generation Systems—Part 1: Design Requirements. International Electrotechnical Commission: Geneva, Switzerland, 2004.
3. Stettner, M.; Reijerkerk, M.J.; Lünenschloß, A.; Riziotis, V.; Croce, A.; Sartori, L.; Riva, R.; Peeringa, J.M. Stall-induced vibrations of the AVATAR rotor blade. *J. Phys. Conf. Ser.* **2016**, *753*, 042019. [CrossRef]
4. Heinz, J.C.; Sørensen, N.N.; Riziotis, V.; Schwarz, M.; Gomez-Iradi, S.; Stettner, M. *Aerodynamics of Large Rotors. WP4. Deliverable 4.5*; Technical Report; ECN Wind Energy: Petten, The Netherlands, 2016. Available online: https://repository.tudelft.nl/islandora/object/uuid%3Af1ee9368-ca44-47ca-abe2-b816f64a564f (accessed on 7 August 2018).
5. Loubeyres, J.; Pfister, J.; Blondel, F.; Guy, N. Stall flutter instabilities on the IEA-15 reference wind turbine in idling conditions: Code-to-code comparisons and physical analyses. *J. Phys. Conf. Ser.* **2022**, *2265*, 032019. [CrossRef]
6. Hansen, M.H.; Gaunaa, M.; Madsen, H.A. *A Beddoes-Leishman Type Dynamic Stall Model in State-Space and Indicial Formulation*; Risoe Report, Risoe-R-1354(EN); 2004. Available online: https://backend.orbit.dtu.dk/ws/portalfiles/portal/7711084/ris_r_1354.pdf (accessed on 1 June 2004).
7. Petot, D. Differential equation modeling of dynamic stall. *Rech. Aerosp.* **1989**, *5*, 59–72.
8. Hansen, M.H. Aeroelastic instability problems for wind turbines. *Wind Energy* **2007**, *10*, 551–577. [CrossRef]
9. Bak, C.; Zahle, F.; Bitsche, R.; Kim, T.; Yde, A.; Henriksen, L.; Hansen, H.; Blasques, J.; Mac, G.; Natarajan, A. Description of the DTU 10MW reference wind turbine. In *Technical University of Denmark (DTU) Wind Energy Report-I-0092*; 2013. Available online: https://dtu-10mw-rwt.vindenergi.dtu.dk (accessed on 1 July 2013).

10. Serafeim, G.; Manolas, D.; Riziotis, V.; Chaviaropoulos, P.; Saravanos, D. Optimized blade mass reduction of a 10MW-scale wind turbine via combined application of passive control techniques based on flap-edge and bend-twist coupling effects. *J. Wind Eng. Ind. Aerodyn.* **2022**, *225*, 105002. [CrossRef]

11. Bagherpour, T.; Li, M.; Manolas, D.; Riziotis, V. Modeling of material bend-twist coupling on wind turbine blades. *Compos. Struct.* **2018**, *193*, 237–246. [CrossRef]

12. Serafeim, G.; Manolas, D.; Riziotis, V.; Chaviaropoulos, P. Lightweight optimal rotor design of a 10MW-scale wind turbine using passive load control methods. *J. Phys. Conf. Ser.* **2020**, *1618*, 022061. [CrossRef]

13. Wu, W.; Cheng, H.; Kang, C. Random field formulation of composite laminates. *Compos. Struct.* **2000**, *49*, 87–93. [CrossRef]

14. Manolas, D.; Riziotis, V.; Voutsinas, S. Assessing the importance of geometric nonlinear effects in the prediction of wind turbine blades loads. *J. Comput. Nonlinear Dyn.* **2015**, *10*, 041008. [CrossRef]

15. Manolas, D.I.; Riziotis, V.A.; Papadakis, G.P.; Voutsinas, S.G. Servo-aero-elastic analysis of floating offshore wind turbines. *Fluids* **2020**, *5*, 200. [CrossRef]

16. Chortis, D.; Varelis, D.; Saravanos, D. Prediction of material coupling effect on structural damping of composite beams and blades. *Compos. Struct.* **2012**, *94*, 1646–1655. [CrossRef]

17. Serafeim, G.; Manolas, D.; Riziotis, V.; Chaviaropoulos, P. Multidisciplinary aeroelastic optimization of a 10MW-scale wind turbine rotor targeting to reducing LCoE. *J. Phys. Conf. Ser.* **2022**, *2265*, 042051. [CrossRef]

18. Virtanen, P.; Gommers, R.; Oliphant, T.E.; Haberland, M.; Reddy, T.; Cournapeau, D.; Burovski, E.; Peterson, P.; Weckesser, W.; Bright, J.; et al. SciPy 1.0: Fundamental algorithms for scientific computing in Python. *Nat. Methods* **2020**, *17*, 261–272. [CrossRef] [PubMed]

19. Popko, W.; Vorpahl, F.; Zuga, A.; Kohlmeier, M.; Jonkman, J.; Robertson, A.; Larsen, T.J.; Yde, A.; Yde, A.; Sætertrø, K.; et al. Offshore Code Comparison Collaboration Continuation (OC4), Phase I—Results of Coupled Simulations of an Offshore Wind Turbine with Jacket Support Structure. *J. Ocean. Wind. Energy* **2014**, *1*, 1–11.

20. Robertson, A.; Jonkman, J.; Vorpahl, W.; Popko, J.; Qvist, J.; Frøyd, L.; Chen, X.; Azcona, J.; Uzunoglu, E.; Soares, C.G.; et al. Offshore code comparison collaboration continuation within IEA Wind Task 30: Phase II results regarding a floating semisubmersible wind system. In Proceedings of the 33rd International Conference on Ocean, Offshore and Arctic Engineering (OMAE), San Francisco, CA, USA, 8–13 June 2014.

21. Veers, P.S. *Three-Dimensional Wind Simulation*; Sandia Report SAND88 0152; Sandia National Laboratories: Albuquerque, NM, USA, 1988.

22. Bortolotti, P.; Berry, D.; Murray, R.; Murray, R.; Gaertner, E.; Jenne, D.; Damiani, R.; Barter, G.; Dykes, K. *A Detailed Wind Turbine Blade Cost Model*; Technical Report NREL/TP-5000-73585; National Renewable Energy Laboratory (NREL): Golden, CO, USA, 2019.

23. Fingersh, L.; Hand, M.; Laxson, A. *Wind Turbine Design Cost and Scaling Model*; Technical Report NREL/TP-500-40566; National Renewable Energy Laboratory (NREL): Golden, CO, USA, 2006.

24. Burton, T.; Jenkins, N.; Sharpe, D.; Bossanyi, E. *Wind Energy Handbook*, 2nd ed.; John Wiley & Sons, Inc.: Hoboken, NJ, USA, 2011; ISBN 978-0-470-69975-1.